

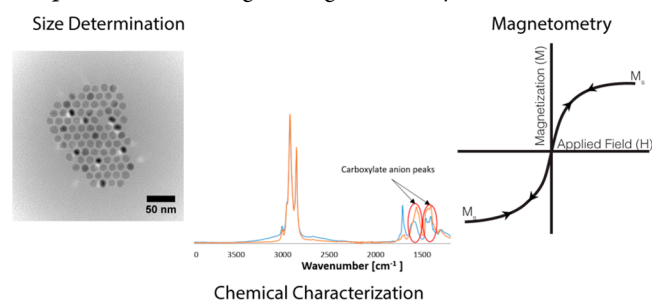
Best Practices for Characterization of Magnetic Nanoparticles for Biomedical Applications

The use of magnetic nanoparticles in biomedical applications provides a wealth of opportunities. Nonetheless, to truly understand the interactions of these materials in biological media, detailed characterization is necessary with these complex systems. This Feature highlights some “best practices” in the analytical techniques and challenges in the measurement of the properties of these materials.

Sarah E. Sandler,[†] Benjamin Fellows,[‡] and O. Thompson Mefford^{*,†}

[†]Department of Materials Science and Engineering, Clemson University, Clemson, South Carolina 29634, United States

[‡]Department of Bioengineering, University of California at Berkeley, Berkeley, California 94720, United States



Magnetic nanoparticles (MNPs) are one of the most often used examples of how nanotechnology can be applied to medical applications. These applications include both imaging (e.g., magnetic resonance imaging (MRI) contrast enhancement agents and magnetic particle imaging (MPI)) and therapy (e.g., magnetic hyperthermia and directed drug delivery).^{1–4} For all of these applications, an understanding of the structure of the particles, the surface functionality, and their resulting magnetic properties are critical for investigators to be able to measure as well as understand the implications of these properties on the medical challenge they are attempting to solve. In order to understand how the function is related to the inherent properties of these particles, characterization is an essential first step.

For better or worse, this field is relatively easy to enter as magnetic nanoparticles can be produced through a number of methods including rudimentary techniques such as aqueous based coprecipitation.^{5,6} Because of this ease of access, there is a wealth of publications with varying degree of characterization and understanding of the material properties that would contribute to the success of the targeted application. In order to translate the technologies of nanoparticles into applications in clinical as well as industrial settings, the challenges of ambiguity in reporting and diversity in measurement must be addressed.

While there have been many review articles that have focused on synthesis, characterization, and applications of magnetic nanoparticles, there is a lack of a concise overview of the methods of characterization and simplified explanation of all aspects of the field relating to MNPs.^{7–10} This Feature is intended for researchers just starting out in the field of magnetic nanoparticles and those who wish to learn more

about the importance of properly characterizing them. The purpose of this Feature is to provide a simple explanation and background on preferred practices in the characterization methods and technologies associated with the MNP field. Specifically covered is the characterization of the dimensionality of these materials, the resulting magnetic properties, surface functionality, as well as application specific characterization techniques. While this Feature provides an overview of these analytical techniques, additional resources are provided throughout. The reader is encouraged to review the recently produced ISO standard on the characterization of magnetic nanosuspensions.¹¹ This ISO catalogs many of the characterization techniques discussed in this Feature.

■ SIZE DETERMINATION

The structure of most MNPs used in biomedical applications can be reduced to two parts: an inorganic crystalline core and an organic shell, as seen in Figure 1. The organic shell is needed to prevent agglomeration of the particles and reduce the potential for a response from the immune system.^{12,13}

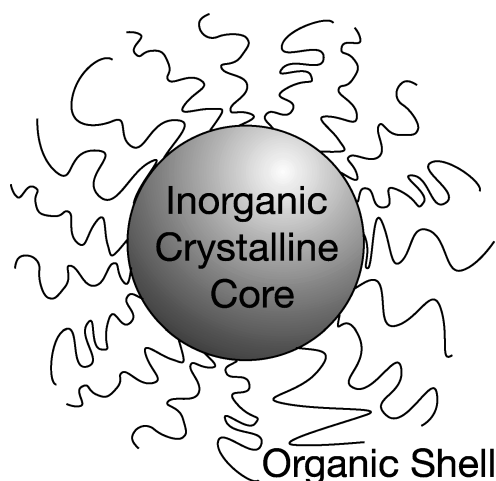


Figure 1. Cartoon illustrating inorganic crystalline core surrounded by an organic stabilizing layer on the surface.

Published: September 30, 2019

Therefore, there are a number of dimensions that need be characterized within the system.

For most biomedical applications, the size of the inorganic core is critical for the success of a given application. For example, particles of relatively small diameters (approximately less than 25 nm for magnetite) are said to be superparamagnetic.¹⁴ Superparamagnetism exhibited for materials with spins within the crystal would normally result in ferro/ferri-magnetism; however, the energy barrier between the different aligned states is less than thermal energy in a given time period. Thus, during the time of measurement the collective moment a system of particles will be measured as zero in the absence of an applied field. In the presence of an applied magnetic field, H , the resulting magnetization, M , can be describe using the Langevin function such that

$$M = cVM_s \left[\coth \left(\frac{VM_s H}{k_B T} \right) - \left(\frac{k_B T}{VM_s H} \right) \right]$$

where c is the concentration of particles, V is the magnetic volume of the particle, M_s is the saturation magnetization, k_B is the Boltzmann constant, and T is the temperature.¹⁵ It is important to note that the Langevin model assumes a “dilute” sample and does not include interparticle interactions.

One possible method to determine particle size is to fit hysteresis loops of particle suspensions accounting for polydispersity of the magnetic core (see magnetic characterization techniques below). For example, Kallumadil et al. demonstrated that the fitting of measurement curves to account for polydispersity within the samples allowed for the comparison of the magnetic crystallite diameters.¹⁶ It should be noted that in order to properly determine if the particles exhibit superparamagnetic behavior, these measurements need to be conducted in a solid matrix. This prevents the particles from physically rotating, as particles suspended in liquid media can freely align with the applied field resulting in curves demonstrating zero hysteresis.¹⁷

Other methods for determining the size of the magnetic core include transmission electron microscopy (TEM), X-ray diffraction (XRD), small angle X-ray scattering (SAXS), and small angle neutron scattering (SANS). SAXS and SANS along with dynamic light scattering (DLS) can also be used to determine the hydrodynamic size of the stabilized particle. Details of each are described below.

The most commonly used method for measuring the core is TEM. TEM provides information about the internal microstructure or ultrastructure of solids rather than just the external structure as scanning electron microscopy (SEM) does.¹⁸ Understanding the internal structure is essential because different core dimensions, coating dimensions, and the ratio between the two result in different behavior of the magnetic nanoparticles. Magnetic nanoparticles have a tendency to agglomerate so sample preparation is essential to get quality images. The samples are prepared by dispersing particles in a chemically inert solution, which does not leave residue and evaporates in a 10–20 min time frame at room temperature. For example, volatile solvents like hexanes can be used for organically stabilized particles. Alternatively, water, with the aid of a heat lamp and desiccant can be used.¹⁹

The major drawback of TEM however is the sample size. Measurements can only be made on a small sample size and is very time-consuming. In addition, as operator bias can influence which images get taken, thus researchers are advised

to avoid introducing subjectivity. In order to get a statistically accurate measurement of the particle diameter, many images should be taken at sufficient magnification to get good contrast between the particles and the background yet zoomed out enough to capture multiple particles in each image. The images can then be analyzed using a program such as ImageJ, which is available for free download by the NIH.²⁰ A good rule of thumb is to measure at least 300 particles to provide sufficient statistical information. Tutorials on how to use the program and analyze images to solve for dimensions can be found on the NIH Web site.²⁰

In comparison to other size determination methods, TEM measures the “real” radius of samples. Since TEM involves desiccation prior to measurement, it only provides information about dry magnetic nanoparticles; however, in many applications particles are typically in colloidal dispersions, which would alter both the size and behavior. Recent advances in liquid based TEM imaging are beginning to show promise to observe particle–particle interactions as well as particle growth in real time.²¹ TEM is typically limited to electron dense material and provides a 2D projection of a 3D particle; thus, other methods are necessary to fully understand particle dimensions. It is possible to also image the outer organic layer, but since it is not solvated, true information regarding its dimensionality is difficult to discern. TEM is also a useful technique to determine cellular interactions with the magnetic particles. Due to the high vacuum environment, special sample preparation is required which involves cell fixing, solvent transfer, staining, microtoming, other advanced procedures.²²

Secondary methods coupled to the TEM provide an opportunity for additional analysis. For example, high-resolution TEM-electron energy loss spectra (HRTEM-EELS) has been used to provide compositional information regarding the compositional nature of core–shell core–shell $\text{Fe}_3\text{O}_4/\text{Zn}_x\text{Co}_{1-x}\text{Fe}_2\text{O}_4$ nanoparticles.²³ The absorption of uranium onto the phosphate-based coating on the iron oxide nanoparticle was observed via energy dispersive X-ray spectroscopy (EDS) of the TEM images.²⁴ In addition, a number of *in situ* allow for the probing with electromagnetic stimuli.²⁵ Finally, one should consider the use of cryogenic-TEM (cryo-TEM) techniques that can preserve the structure of aqueous or biological media. For example, cryo-TEM has been used to observe the nucleation and growth of coprecipitation particles,²⁶ the structure of magnetoliposomes,²⁷ and changes to the aggregation state when interacting with cells.²⁸

Also known as wide-angle X-ray scattering (WAXS), XRD allows researchers to determine information with respect to the crystalline ordering of the atoms in magnetic core. As the crystalline core is responsible for the magnetic response of these materials, understanding the atomic ordering is critical to the success of most applications. Much information can be gained from XRD, including the structure of the crystals, lattice spacing, and size of the crystallites.⁷ The size can be determined from measuring the broadening of the peaks of the spectrum using the Scherrer equation such that

$$D = \frac{0.9\lambda}{\beta \cos \theta}$$

where D is the crystalline size (nm), λ is the wavelength of the X-ray source, β is the width at half height of the peak accounting for instrumental broadening, and θ is the wavelength of the peak (typically the largest in the spectrum).

While the Scherrer equation offers a convenient route to measure crystalline particle sizes, it has its limitations for noisy data where more advanced integration based methods offer the ability to better interpret the data and account for peak broadening from crystalline size and strain.^{29,30} This results in the Williamson–Hall equation:

$$D = \frac{0.9\lambda}{\beta \cos \theta} + 4\epsilon \sin \theta$$

where ϵ is the strain within the particles. One additional option to determine size information from XRD is the size-strain plot (ssp) method, which benefits from weighting lower angles over higher angles.³¹

When using XRD for structural identification, the reader is cautioned that both magnetite (Fe_3O_4) and maghemite ($\gamma\text{-Fe}_2\text{O}_3$) are inverse spinel structures, and the resulting XRD spectrum is nearly identical; thus, XRD is not an accurate method to discern between the two species. This fact is rather unfortunate, as these materials represent the bulk of the current literature. Alternative methods to distinguish between these two include Mössbauer spectroscopy at cryogenic temperatures, observing the Verwey transition of magnetite, or potentially TEM-EELS in the context of either XRD or Raman spectroscopic information.^{32,33}

SAXS as well as other low-angle scattering techniques (medium angle and ultrasmall angle) have become integral in the characterization and study of nanoscale materials.⁸ In a typical experiment, a sample is irradiated with a high-flux X-ray beam. This beam is scattered by the sample, and the scatter profile at variable angles (inversely proportional to distance) are collected. Because of this inversely proportional relationship with distance, typical investigation angles range from 0.1° to 5° . Unlike other methods where the morphology and structure of nanomaterials can be obtained (i.e., electron microscopy), X-scattering samples a macroscopic region to give averaged structural data of the materials in question. SAXS is also unique in its ability to probe mesoscale ordering and self-assembly in native solutions of dispersed nanoscale colloids.⁸ Here is where a large deal of utility is found over many electron microscopy techniques as it is notoriously difficult to maintain in situ structural information in electron microscopy without introducing artifacts from sample preparation. This is not to say that X-ray scattering is the ideal technique, as the extraction of both the form factor and structure factor require assumptions in geometry, dispersity, and interparticle interaction. As the complexity of these assumptions increases (e.g., dilute solution of monodispersed hard spheres to interacting agglomerates of multiple length rods), it may be necessary to introduce approximations into the mathematical treatment of the particle scattering.³⁴ Two common approximations used in literature for more complex systems are the decoupling approximation which assumes that the intrinsic properties of the particles are not correlated with their positions, and the local monodisperse approximation which assumes that locally, all particles are identical. It is of the utmost importance that these approximations be carefully considered misinterpretation of obtained scattering data if they cannot be reasonably fulfilled.

The form factor is of high importance, as its analysis provides insight into the size distribution of the sample as well as the particle shape. Typically, some a priori assumption of the nanoparticle geometry or distribution are used in the form

factor model as it is necessary to know or assume one to find the other. This is seen in the form factor equation

$$P(q) = \int n(R) \langle |F(q, R)|^2 \rangle dR$$

where $n(R)$ is the size distribution function, and $F(q, R)$ is a function defining particle shape. Using a model-based approach and assuming a functional form of $n(R)$, it is possible to analytically solve for both the number-averaged radius of the particles as well as the root-mean-square deviation of the distribution. As stated previously, as a particle system becomes increasingly complex, the mathematical treatment of the scattering also becomes more complex. Today, the form factors of “simple” shapes have been worked out and are typically available from various libraries or software packages.³⁵ Multiple studies on monodisperse nanoparticle solutions have compared nanoparticle size using TEM, SAXS, and XRD. Each method has been shown to agree and can each be used to characterize size dispersions of nanoparticles.³⁶

One of the unique capabilities of SAXS is the ability to investigate superstructure assemblies of nanomaterials and their structures *in situ*.^{37,38} Typically, this is done by analyzing the structure factor which defines the interparticle distance (similar to the interatomic distance in X-ray diffraction). As with the form factor discussed before, difficulties arise in decoupling the form and structure factor when particles are not assumed to be monodispersed spheres. There is a large swath of literature discussing the mathematical approaches to characterizing more complex materials and their assemblies. The ability to elucidate the mesoscale structural components of nanoparticle suspensions is of particular importance with magnetic nanomaterials, as the addition of a large magnetic dipole may cause small scale ordering of these materials.^{39,40} SAXS in itself is a powerful and unique tool for exploring solution dynamics of nanoparticles. Its ability to probe the nanoscale properties of a bulk solution without worry of bias is essential for adequate characterization of nanoscale dispersions of all types of materials.

SANS is also a highly useful technique to determine the microstructure on the order of 1–300 nm. One of the major benefits to SANS is that experiments can be conducted in a variety of sample environments including variable temperature and pressure as well as in the presence of electric and magnetic fields.⁴¹ In addition to information about the inorganic core, SANS can be used to measure the density of the stabilizing polymeric brush.⁴² More recent advancements in SANS have utilized polarized neutrons to reveal field induced uniform spin canting on the surface shell of the magnetite nanoparticle.^{43,44}

MNPs are typically prepared and used for application in the form of colloidal dispersion, which makes dynamic light scattering (DLS), also called quasi elastic light scattering (QUELS), an easy and essential size measurement technique. DLS is a very popular method because of the noninvasive and quick and simple nature of the measurements. DLS measures the fluctuations of the light scattered by dilute colloidal suspensions allowing for determination of a particle Brownian motion relative to a given hydrodynamic radius (r_H).⁹ This radii takes into account the effect of drag between the particle and the liquid it dispersed. Measurement of this size is essential in describing the colloidal stability of these materials in varying environments, particle–particle interactions and aggregation, and the degree of surface modification of the MNPs.^{13,45,46}

The Brownian motion can be described by the Stokes–Einstein equation:

$$D_T = \frac{k_B T}{6\pi\eta r_H}$$

where D_T is the translational diffusion coefficient, k_B is the Boltzmann constant ($1.380 \times 10^{-23} \text{ kg m}^2 \text{ s}^{-2} \text{ K}^{-1}$), T is the temperature in Kelvin, and η is the viscosity of the suspending media. Thus, larger particles will have slower diffusion rates compared to smaller particles. Through a process of correlating the intensity of scattered photons at various time points, the corresponding decay in correlation is used to determine the diffusion rate for the particles, where smaller particles will have a faster decay in correlation compared to larger particles. The resulting correlation function is then fitted through use of an algorithm like the commonly used constrained regularization method for inverting data (CONTIN), which assumes a logarithmic distribution of particle sizes.^{47,48}

DLS typically can provide four different outputs: Z-average diameter (αr^6), intensity-weighted diameter (αr^6), volume-weighted diameter (αr^3), and number-weighted diameter (αr^1). The intensity weighted diameter is the raw data from the scattering intensity of each particle fraction, the number and volume are deduced from the intensity weighted, and the Z-average is the “cumulant mean”. The Z-average is the most popular way to report the diameter measured by DLS, because of the reliance of the technique on least-squares fitting and thus an insensitivity to noise.⁴⁹ Because scattering is a weighted measurements and measures particles as a function of the radii to the sixth power, it is very sensitive to agglomerates of particles. New investigators are often tempted to report only number-average results, which will typically show the smallest size and distribution in an effort to claim monodisperse particle distributions. Unfortunately, this form of selection bias should be avoided by reporting the various fits of the data.

When measuring size based on DLS using MNP samples, it is important to take concentration into consideration. With too low of a concentration, such as 0.1 mg/mL sample, there may not be enough scattering of the light occurring to accurately measure the sample. However, with too concentrated of a sample such as 100 mg/mL, multiple scattering occurrences may occur leading to inaccurate results.⁵⁰ A good reference is ISO 22412:2017(E), which provides a comprehensive view on sample preparation and analysis.⁵¹

One should also consider the dispersing media for DLS measurements. While it may be convenient to demonstrate particle stability in ultrapure water, this does little to suggest the colloidal stability of these materials in the biological environment. More representative media includes solutions that mimic the ion concentration and osmolarity of the human body, such as phosphate-buffered saline. To test stability in protein rich media, supplements like bovine serum albumin are a convenient choice. Also useful for assessing the colloidal stability of these materials in different media is nanoparticle tracking analysis, where the motion of the particles is captured with a camera the Brownian motion is calculated on a particle-by-particle basis. This allows for the observation of stability in biological media⁵² or the natural environment.⁵³

Zeta-potential measurements are often conducted on the same instrumentation as DLS. Often the results of these measurements are used to determine particle stability based off of electrostatic repulsion between particles. Zeta-potential is

not directly measurable, rather it can be determined through charge potential generated motion (i.e., electrophoretic mobility). Typical measurements are conducted in a U-shaped sample holder with electrodes located at the top two ends. An alternating voltage is applied to the suspension of particles resulting in electrophoretic mobility of charged particles. This motion is measured changes through phase shifts in the scattered intensity. As zeta-potential describes both the surface charge of the particles in a given medium, careful attention must be made to ensure that the materials remain fully in suspension during the entire measurement. This includes control over the pH and specific ion concentration of the suspending media, including precaution to ensure the effects of sample dilution do not alter the surface charge of the particles.⁵⁴

■ CHEMICAL CHARACTERIZATION

Given that these materials are designed for biomedical applications, authors are strongly encouraged to provide a comprehensive reporting of the chemical composition of the inorganic core and the organic shell. Of critical importance is the surface chemistry of the particles, which defines the way in which they interact with both one another and their environment. Often magnetic nanoparticles are produced with one ligand and replaced by another that provides the necessary functionality (e.g., steric stability, disease specific targeting, and opportunities for additional modification).⁵⁵ Key questions that must be answered via chemical characterization include What is the concentration of magnetic particles in a suspension? How successful was the ligand exchange in altering the surface chemistry? and What is the surface coverage of the ligand on the surface?

Concentration of particles in suspension is important to know for both additional magnetic characterization (see below) or knowing the amount of material added to cells or animal subjects. As the majority of research in this field is centered on iron oxide materials, one convenient method is the use of UV–vis spectroscopy to measure the concentration of iron in a sample. The preferred method involves first dissolving the particles in concentrated hydrochloric acid and the oxidative state of the iron can be reduced with hydroxylamine hydrochloride. Next the iron is complexed with 1,10-phenanthroline and resulting in absorbance at approximately 510 nm. The resulting absorbance can be compared to known samples to create a standard curve.⁵⁶ If detection of iron at lower concentrations or multiple elements need to be measured, inductively coupled plasma (ICP) equipped with either a mass spectrometer (MS) or atomic emission spectroscopy (OES) are used. Readers are encouraged to read previous *Analytical Chemistry* articles describing elemental analysis.⁵⁷

For determining the amount of organic material on the surface of the particle, the most commonly used method is thermal gravimetric analysis. In a typical experiment, the weight loss is measured from slightly above 100 to 500 °C at a rate of 10 °C/min purging with nitrogen. It is important to remove all residual solvent (i.e., water or other) prior to this measurement, so an isothermal hold at 100 °C prior to the measurement is necessary. The char yield of the organic layer must be accounted for as well. This requires a secondary experiment with just the organic material. Knowing the weight loss, the size distribution of the inorganic core (typically from TEM), and the char yield of the organic layer, one can

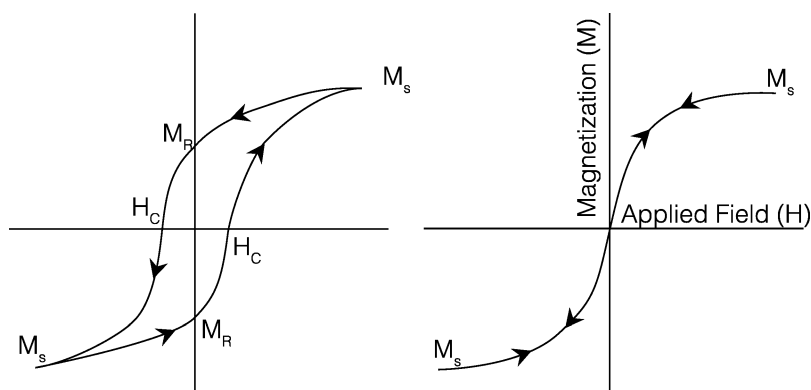


Figure 2. Representative M – H loops of (left) magnetic nanoparticles exhibiting hysteresis and (right) where no hysteresis is observed.

determine the number of chains per nm^2 on the surface of the particles.^{58,59} While convenient, one is cautioned with this method as it assumes that only one species of organic material is on the surface of the particles. As recently shown by Davis et al. via radioanalytical techniques, commonly used ligand exchange reagents and methods do not completely remove sacrificial ligands such as oleic acid.^{60,61}

For chemical identification of the moieties on the surface, one is tempted to utilize nuclear magnetic resonance (NMR) spectroscopy. Unfortunately, the magnetic particles create large field inhomogeneities resulting in peak broadening rendering images indiscernible. A better option is the use of Fourier transform-infrared (FT-IR) spectroscopy, which measures the vibrational energy of the bonds. Samples can be prepared through a multitude of methods. Most common include the preparation of particles dispersed in potassium bromide (KBr) pellets for transmission analysis or measurement via attenuated total reflectance (ATR).^{24,58,62–64} In a typical FT-IR spectrum of iron oxide nanoparticles, there will be at least two well-defined peaks at 577 and 631 cm^{-1} , due to the presence of iron–oxygen (Fe–O).⁶⁵

In addition to FT-IR, there is Raman spectroscopy (RS) and X-ray photoelectron spectroscopy (XPS) which are useful in crystal phase determination. Raman spectroscopy is useful for chemically characterizing ferrite particles in particular because of the sensitivity to cation disorder, the possibility to identify different oxides phases like hematite or magnetite, the ability to monitor the stability of spinel ferrites vs light exposure or thermal treatment, the effect of nanometric scaling on Raman lines features such as peak energies, widths, and shape, and the opportunity to evaluate the presence of unwanted impurities.⁶⁶ In RS, two common lasers used are 514 and 785 nm, which will produce different characteristic peaks. The characteristic peak of magnetite is 654 cm^{-1} with a 514 nm laser but is 670 cm^{-1} by a 785 nm laser, which can be due to possible oxidation into maghemite because of the higher power.⁶⁷ Additionally, XPS is useful for nanoparticulate characterization because the energies of emitted photoelectrons are characteristic of both elements and the oxidation state.⁶⁸

■ MAGNETISM

The magnetic properties of these materials are what makes these materials unique. Those new to the field are often tempted to demonstrate that their materials are magnetic through pictures of vials with permanent magnets pulling magnetic material to the side. While this may make a good image demonstrating a magnetic response, it also demonstrates poor

colloidal properties of your suspension, meaning that your material is not properly modified and is not stable in the media presented. Rather, authors are encouraged to utilize more quantifiable characterization methods like those described below. The reader is encouraged to consult other reviews for more specific details on experiments.¹⁷

The first property of concern is often the magnetization (M) as a function of an applied field (H). The relationship between these vectors is used to describe the magnetic flux (B), such that

$$B = \mu_0(H + M)$$

where μ_0 is the permeability of free space.⁶⁹ In order to experimentally characterize this relationship, there are several different methods that can be used. One of the most common ways to describe magnetic behavior of a material is using direct current (dc) magnetometry techniques. In dc measurements, the field is uniform and constant, thus the samples must be physically moving in order to produce a change in the magnetic field. One way to measure the moment by force is using a vibrating-sample magnetometer (VSM). Using a VSM, a sample is placed in a copper coil with an applied field and then vibrated perpendicular to the field and the magnetic moment is recorded by measuring a change in voltage.⁷⁰ Simple and relatively inexpensive, it is reliable providing information about the magnetic moment of a material as a function of temperature, field, and crystal orientation.⁷⁰ However, discovered in 1959, the VSM while a fast way to measure, has a relatively poor sensitivity compared to more recent characterization methods such as superconducting quantum interference devices (SQUID). The output voltage of a SQUID is recorded in the form of a flux profile and provides valuable information about the magnetic properties of a material.⁷¹ Another way to measure the magnetic properties of particles can be done using hybrid VSM SQUID equipment.

In preparing samples for this measurement, it is important to prevent unintended particle rotation. Several methods can be adopted to accomplish this goal. Perhaps the simplest is suspending the particles in a media that will be a solid at measurement temperatures. For example, samples in water can be made below the freezing point or organic media such as wax at room temperatures.⁷² An improved method is suspending the particles in a cross-linkable polymer matrix as best described by Maldonado-Camargo et al.¹⁷ Briefly, materials that are intended for aqueous media can be suspended in tetraethylene glycol dimethacrylate and then cross-linked. Organic suspendable particles can be cross-linked in styrene

and divinylbenzene. One final method is drying particles on a matrix such as a cosmetic cotton swab. One should be advised to purchase high-quality swabs as iron filings (from processing the cotton) can often appear in the swab, thus limiting the accuracy of the measurement. Finally, following the measurement, the concentration of materials will need to be determined using methods described above.

Superparamagnetic materials are characterized by their lack of a hysteresis loop.⁷³ Hysteresis loops are magnetization curves that represent a materials magnetic behavior of the multiple domains as can be seen in Figure 2. Since all the domains do not return to their original orientations after the magnetic saturation (M_s) is reached and the field is decreased, there is remnant magnetization (M_R). M_R can be removed by applying a magnetic field in the opposite direction to the original applied field, which is defined as the coercive field (H_c). Superparamagnetic nanoparticles only possess a single domain; they do not exhibit a hysteresis loop as ferromagnetic and ferromagnetic materials do. Depending on the type of magnetism the material possesses, there is another intrinsic property that relates to the order and alignment of the magnetic domains. For ferromagnetic and ferromagnetic substances, the Curie temperature (T_c) describes the transition between order and disorder for the domains, where for antiferromagnetic materials the Néel temperature (T_N) describes this change.⁷³ Beyond T_c or T_N , a material loses its magnetization as a result of the disorder. Superparamagnetic materials, however, are characterized by a blocking temperature.

In addition to hysteresis loops performed through traditional methods such as VSM, there is a growing trend in measuring the hysteresis as a function of frequency through dynamic hysteresis loops. While VSM does offer a good bit of information about the magnetic structure of the particles, for many applications where an ac field is applied, the measured coercivity is not applicable. For example, ac hysteresis in fields in the range of 4–24 kA/m at 100 kHz can be measured through some recent advances in instrumentation.^{74–77} This allows one to determine the effect of frequency on the hysteretic behavior of these materials.

Field cooling (FC) and zero field cooling (ZFC) are experimental ways to measure the response of a material based on its anisotropy in order to obtain information about blocking temperatures.^{78,79} Using these methods, one can differentiate between different types of magnetism.⁸⁰ In both methods, particles are experimentally cooled below their blocking temperatures and magnetic behavior is recorded; the difference is the presence or lack thereof an applied field. In ZFC, the magnetic moment is frozen along the easy direction, where in FC the magnetization is frozen in a different direction depending on the anisotropy of the particles. From this information, one can gather information about the distribution of blocking temperature and thus the energy barriers.

For single domain particles, changes in the direction of magnetization of MNPS is modeled in two ways: Brownian Relaxation and Néel Relaxation. Both the time Brownian and Néel relaxation time constants include volume and can be modeled by the following:

$$\tau_B = \frac{3\eta V_H}{k_B T}$$

$$\tau_N = \tau_0 \exp \frac{K_{\text{eff}} V_m}{k_B T}$$

$$\frac{1}{\tau} = \frac{1}{\tau_N} + \frac{1}{\tau_B}$$

where τ_B is the Brownian relaxation time, τ_N the Néel relaxation time, V_H the hydrodynamic volume, V_m the volume of the magnetic core, η the viscosity of the suspending media, k_B the Boltzmann constant, T is the temperature in Kelvin, K_{eff} is the effective magnetic anisotropy, and τ_0 is the attempt frequency (typically assumed to be 10^{-9} s). The Brownian relaxation depends on the hydrodynamic volume and is a fluid dependent representation of the magnetic behavior of particles, whereas the Néel relaxation time is dependent on the magnetic anisotropy. Brownian relaxation time is concerned with physical particle rotation due to Brownian motion, whereas Néel relaxation characterizes rotation of the magnetic field within the particle and not the particle itself. When $\tau_N \ll \tau_B$, the primary mechanism is Néel relaxation; however, when $\tau_N \gg \tau_B$, particles follow the Brownian mechanism.⁸¹

As seen above, the Brownian relaxation time will scale with the hydrodynamic volume, leading toward the potential for bioassays.⁸² One way to measure these changes in hydrodynamic volume is through dynamic magnetic susceptibility (DMS) or ac susceptibility. This analysis is done via a small-amplitude alternating magnetic field (H) applied to colloidal suspensions of nanoparticles. One can describe the change of magnetization (M) as a function of time (t) as^{83,84}

$$\frac{dM}{dt} = \frac{1}{\tau}(M - \chi_0 H)$$

where τ is the relaxation time of the particle and χ_0 is the linear susceptibility at low fields. If one were to describe the alternating field with a frequency (ω), such that $H(t) = H_0 \cos \omega t$, the resulting magnetization of the particle would take the form:

$$M(t) = \chi' H_0 \cos(\omega t) + \chi'' H_0 \sin(\omega t)$$

where χ' is the in phase (real) portion and χ'' is the out of phase (imaginary) portion. Utilizing Debye theory and accounting for background susceptibility, the infrequency susceptibility (χ_∞) is used to describe χ' and χ'' such that⁸³

$$\chi' = \chi_\infty + \frac{\chi_0 - \chi_\infty}{1 + \omega^2 \tau^2}; \quad \chi'' = \frac{(\chi_0 - \chi_\infty) \omega \tau}{1 + \omega^2 \tau^2}$$

As frequency increases, χ' approaches the asymptote χ_∞ . χ'' will, however, have a peak value when $\omega \tau = 1$. Thus, by monitoring changes in this peak frequency, the team will measure changes in the hydrodynamic diameter of the particles as a function of temperature⁸³ and interactions with proteins,⁸⁴ estimate the Néel and Brownian contributions,⁸⁵ determine whether the particles are aggregated or not,^{17,84} determine whether the structure of the particle is single or multicore,⁸⁶ and detect bioconjugation.⁸⁷

When calculating the Néel relaxation time and the blocked temperature, the concept of magnetic anisotropy is often brought up. Magnetic anisotropy relates the crystal structure and shape of the grains based on the different domains to the magnetization direction. Magnetic properties rely heavily on

direction, which makes the anisotropy important because of the effect it has on hysteresis loops and coercivity. The coercivity of a material is the resistance to changes in magnetization, which is essential for understanding and predicting the properties of MNPS. There are different types of anisotropy, such as magnetocrystalline anisotropy and shape anisotropy.⁶⁹ Magnetocrystalline anisotropy is an intrinsic property based upon the relationship between the direction of crystallinity, the temperature and the magnetization. For example, at different crystal directions such as $\langle 111 \rangle$, $\langle 100 \rangle$, and $\langle 110 \rangle$ at a certain temperature, materials will express different magnetic saturations.⁶⁹

As described in the introduction, the difference between measuring magnetite and maghemite in samples is essential to the understanding. Magnetite and maghemite both possess inverse spinel structures with their oxygen layers in an FCC-type stacking along the $[111]$ direction.⁸⁸ Magnetite, Fe_3O_4 , has full occupancy of these sites in the form of $\text{Fe}^{3+}[\text{Fe}^{2+}\text{Fe}^{3+}]\text{O}_4$. When the ferrous ions are measured using spectroscopy techniques, such as Mossbauer spectroscopy, the $[\text{Fe}^{2+}\text{Fe}^{3+}]$ behave as $\text{Fe}^{2.5+}$ because of the fast electron hopping.⁸⁸ The ferrous ions in samples of maghemite however all get oxidized from Fe^{2+} to Fe^{3+} , which in turn results in different results in both the number and positions of absorption lines when using ^{57}Fe Mossbauer spectroscopy. Mossbauer spectroscopy is a useful way to distinguish between magnetite and maghemite in iron oxide particles, which will become more and more relevant in application purposes. The reader is encouraged to utilize the manuscript by Fock et al. for further analysis.⁸⁸

One of the enticing properties of iron oxide nanoparticles that brings new researchers into the field is their ability to be used as magnetic resonance imaging contrast agents. That is, they are able to shorten the protons T2 (transverse) and T1 (longitudinal) relaxation times. Commonly, due to the large magnetic inhomogeneity created, magnetic nanoparticles are referred to as T2 shortening agents with relaxivity values ($\text{mM}^{-1} \text{s}^{-1}$) in the 100 s.⁸⁹ Relaxivity measurements are typically done in either a dedicated relaxometer, NMR, or MRI. Typically for a T1 measurement, an inversion recovery pulse sequence is used consisting of a 180° pulse, a variable delay, and a 90° readout pulse.⁹⁰ Obtained data is typically fit to an exponential, and the T1 can be extracted from the fit. The measurement of T2 and T2* use very different pulse sequence than the inversion recovery, commonly referred to as a CPMG (Carr–Purcell–Meiboom–Gill) sequence or a spin echo sequence. This uses a 90° pulse followed by subsequent 180° pulses to refocus dephasing spins, creating a decaying “echo” as the pickup signal. Because of field inhomogeneities, apparent T2 relaxation when measures with a single exponential decay signal are much faster than predicted. This phenomenon is referred to as T2* and is an important parameter separate from T2.⁹¹ To get a true T2 measurement, multiple spin echoes must be done. The amplitude decay is “free” of the magnetic inhomogeneities causing the apparently increased relaxation velocity seen in T2* and is therefore a true measure of T2.⁹² Typically the relaxivity of a contrast agent is reported, which is a concentration normalized value ($\text{mM}^{-1} \text{s}^{-1}$). This is generated by taking multiple T1 or T2 measurements at varying concentrations, taking the inverse to get a frequency value, and linearly fitting the data set. The slope of this fit is the concentration normalized relaxivity. The ability of magnetic nanoparticles to be used as MRI contrast agents is an exciting application which allows them to be

biologically tracked, used in theranostic applications (hyperthermia/MRI), and tuned to create responsive sensors of dynamic processes *in vivo* due to changing relaxivity values.⁹³

In 1979, Gordon et al. first proposed the use of magnetic nanoparticles for the heating and destruction of cancerous cells.⁹⁴ A similar approach is still used today in which either ferromagnetic or superparamagnetic particles are placed in proximity to targeted cells. The targeted tissue is then exposed to an alternating magnetic field (AMF). The particles convert the magnetic energy to phonons which can result in increased thermal energy. Traditionally, the mechanism of cell death was attributed to the bulk heating of the tissue above tolerable temperatures, hence the frequent use of the term “magnetic hyperthermia” which is still used in the literature and accepted by many researchers. This technique has been shown effective for the removal of osteosarcoma cells in hamsters⁹⁵ and T-9 rat glioma cells.^{96,97} A German based firm, which has a clinical system to deliver the alternating field for use in human subjects, has also recently reported successful treatment of prostate and brain cancer with their device.^{98–101} However, recent findings indicating the possibility that cell death may be possible without cell heating has now resulted in a reevaluation of the previous assumptions regarding temperature effects.^{102–108} Specifically, energy conversion rather than bulk heating should be the focus. Author Mefford along with others¹⁰⁹ have led an effort to adopt the term magnetically modulated energy delivery (MagMED) to distinguish their work from that focused on thermal therapy. Like magnetic hyperthermia, the goal of MagMED is to induce cell death. However, in MagMED thermal effects are not the driving force. Rather, it is hypothesized that the phonons released with every cycle of the alternating field interact with cellular functions that can result in the disruption of the cell membrane, the induction of apoptosis signaling cascades, or other such mechanisms to promote cell death. Other alternative theories include the formation of reactive oxygen species and thermophoresis. Central to all of these theories is the need for efficient conversion of the alternating energy, which is the focus of this project.

The amount of energy released by a magnetic system during a single cycle of an oscillating applied magnetic field is given by¹¹⁰

$$U = \int_{-H_{\max}}^{H_{\max}} \mu_0 M(H) dH$$

where H is the applied field and M is the component of the total magnetization along the applied field axis. As explained in the magnetic review, the plot of $M(H)$ is called a “hysteresis” curve. The energy output, U , is equal to the volume enclosed by the curve. U depends on the oscillating field frequency f and on the properties of the magnetic particles. For applications, the specific absorption rate (SAR) is sometimes referred to as specific loss power (SLP). SAR, the rate of energy production, is important and is given by $\text{SAR} = U^*f$, where f is the frequency of the applied oscillating field and is often reported in units of watts of energy per gram of particles $[\text{W/g}]$. This value, however, does not account for differences in field and frequency, which vary widely in the current field of research. The effect of magnetic field is more complex, as the resulting magnetic moment of a particle is nonlinear with respect to the applied field. Moreover, the hysteresis loops observed using traditional magnetometry (i.e., superconducting quantum interference devices (SQUID) and vibrating sample magneto-

meters (VSM)), have measurement times in the range of 7 orders of magnitude different than those used in magnetic hyperthermia. This difference is important as materials that appear to have no hysteresis in a traditional VSM loop are observed to have significant coercivity at relevant frequencies.¹¹¹ Thus, as the field amplitude is increased, there is an “opening up” of the hysteresis loop.^{110,112–114} Thus, at the typical frequencies of MagMED, increasing the field yields a larger area of the hysteresis loop resulting in greater energy conversion. This trend will continue until one approaches the saturation magnetization of the particles.¹¹⁵

It is tempting when pursuing a high SAR value to increase the frequency to a high value and the field near the saturation magnetization of the magnetic particle. Regardless, the heating limitations the frequency and field applied to tissue must be carefully considered. Exposure to high frequency has been shown to produce dangerous physiological responses.¹¹³ This effect is mainly due to the firing of nerve synapses, resulting in the stimulation of muscles. This undesired nervomuscular response can result in cardiac arrhythmia and other disorders.¹¹³ It has been suggested that frequencies be kept less than 200 kHz as well as the product of the field and frequency be no greater than $4.85 \times 10^8 \text{ A m}^{-1} \text{ s}^{-1}$.¹¹⁶ While a useful guide, this value was determined by severe extrapolation, and thus the true effects of field and frequency will depend on the particles and media.¹⁰⁹

The resulting hysteresis loop is a derivative of the particles that relax to realign with the alternating magnetic field. The area of this hysteresis is the total magnetic energy lost (postulated to be in the form of phonon release) in each cycle due to the particles responding to the changing field. This response is typically described by two different mechanisms: (i) the internally switching of the direction of the particle's magnetization to align with local fields or (ii) the physically rotation to reach realignment with applied field. These are known as Néel and Brownian relaxation, respectively, and were described previously in the size characterization section of this Feature.

When it comes to characterizing and defining a value to the potential of the particles, the SAR is used to report data. The SAR value can be defined as

$$\text{SAR} = C_p \frac{m_s}{m_p} \frac{dT}{dt}$$

where C_p is the heat capacity of the measured suspension, m_s is the mass of the suspension, m_p is the mass of the particle in the sample, and $\frac{dT}{dt}$ is the change in temperature over time.^{109,117}

Although SAR values are commonly reported, different groups use different methods to calculate it. As mentioned before, the frequency of the field used can often change the results of the SAR; however, this is typically reported with the results. Another major difference between research groups is the method to calculate the change in temperature per time to use in the equation. Most commonly used is the initial slope method. In this method, the sample change in temperature per time is recorded starting at a baseline temperature for a small period of time and the initial slope of the heating is recorded and reported. However, different groups have used different ways to calculate the initial slope, which leads to discrepancies in reported results.¹¹⁸

For this reason, it is important to be skeptical and carefully read the literature to determine how the SAR value was

calculated before accepting one synthesis method or size as more efficient than another. While other groups may use more complicated methods or computer programs to calculate the change in temperature per time, ultimately, studies have shown there is not much difference from when the SAR value is calculated using the much simpler initial slope correctly. If delayed heating effects are accounted for and the slope is calculated where there is initially a linear curve (for the first 40 s or so), then there is not much difference observed in the results.

Another concept worth mentioning is the intrinsic loss parameter (ILP). Some groups are beginning to report this rather than the SAR because it removes the impact of field and frequency in the calculation. The ILP can be defined as

$$\text{ILP} = \frac{\text{SAR}}{fH^2}$$

The ILP is only considered constant in relatively low field strength and low frequency measurements because of the field and frequency dependence of χ'' .¹¹⁹ Due to this issue, ILP is not recommended for use as a comparative tool between studies. In order to properly compare the SAR performance between samples, the field, the frequency, measured concentration, and media all need to be held constant.

CONCLUSION AND OUTLOOK

This Feature has presented the basic building blocks on how to best report one's findings when developing new magnetic nanoparticles for biomedical applications. That is, one could create a simple check list to ensure they are best describing these materials. Essential elements include quality TEM with a sufficient number of particles to describe the size distribution of the inorganic core, quantification of the surface coverage of any surface modification, DLS measurements in representative media to demonstrate colloidal stability, and $M-H$ loops performed in a solid matrix to observe the saturation magnetization and any presence of hysteresis. This should then be followed by application specific characterization that test the particles in media that is representative. For example, experiments should be run in media with similar ionic strength and viscosity as these could impact the aggregation and magnetic relaxation of the particles.

Beyond the scope of this Feature are the interactions of these materials in the biological environment. Ultimately, this is where the true application of these materials will be tested. The reader is encouraged to explore one of the many excellent review articles on this subject.^{120,121} Nonetheless, the same philosophy of fully characterizing the effects of these materials should be taken.

There is great potential for the application of these materials. Through careful examination of the material properties, one can make meaningful conclusions of causal relationships driving better science. It is hoped that this Feature can be a guide to elevate the field to new possibilities.

AUTHOR INFORMATION

Corresponding Author

*E-mail: mefford@clemson.edu.

ORCID

O. Thompson Mefford: 0000-0002-9164-2521

Notes

The authors declare no competing financial interest.

Biographies

Sarah E. Sandler recently completed her Bachelor of Science in Material Science and Engineering at Clemson University. Her research interests include the metrology and biomedical applications of nanotechnology. Her research focus has been on the physical, electrical, and magnetic properties of magnetic nanoparticles.

Benjamin Fellows is a postdoctoral scholar in the Berkeley Imaging Systems Laboratory at the University of California, Berkeley. His research interests include the synthesis of novel magnetic materials and their application in medical imaging, biosensing, and theragnostics. Currently his research is focused on the development of novel iron oxide tracers for magnetic particle imaging.

O. Thompson Mefford is an Associate Professor in the Department of Materials Science and Engineering at Clemson University. His research focuses on developing stable, polymer-iron oxide nanoparticle complexes and composites for biomedical applications. These applications include developing materials for magnetically modulated energy delivery, MRI contrast agents, and drug delivery systems.

ACKNOWLEDGMENTS

This Feature stemmed from discussions among colleagues following the Frontiers in Biomagnetic Particle meeting in 2013 (magneticnanoparticle.com). The authors would like to thank the many fruitful discussions with Jennifer Andrew, Thomas Crawford, Lucia Gutierrez, Dale Huber, Urs Hafeli, John Moreland, Carlos Rinaldi, and Tim St. Pierre.

REFERENCES

- (1) Majetich, S.; Wen, T.; Mefford, O. T. *MRS Bull.* **2013**, *38*, 899–903.
- (2) Pankhurst, Q. A.; Connolly, J.; Jones, S. K.; Dobson, J. J. *J. Phys. D: Appl. Phys.* **2003**, *36*, R167.
- (3) Pankhurst, Q. A.; Thanh, N. K. T.; Jones, S. K.; Dobson, J. J. *J. Phys. D: Appl. Phys.* **2009**, *42*, 224001.
- (4) Krishnan, K. M. *IEEE Trans. Magn.* **2010**, *46*, 2523–2558.
- (5) Lefebure, S.; Dubois, E.; Cabuil, V.; Neveu, S.; Massart, R. *J. Mater. Res.* **1998**, *13*, 2975–2981.
- (6) Massart, R. *IEEE Trans. Magn.* **1981**, *17*, 1247–1248.
- (7) Mourdikoudis, S.; Pallares, R. M.; Thanh, N. T. K. *Nanoscale* **2018**, *10*, 12871.
- (8) Li, T.; Senesi, A. J.; Lee, B. *Chem. Rev.* **2016**, *116*, 11128–11180.
- (9) Carvalho, P. M.; Felício, M. R.; Santos, N. C.; Gonçalves, S.; Domingues, M. M. *Front. Chem.* **2018**, *6*, 237.
- (10) Colombo, M.; Carregal-Romero, S.; Casula, M. F.; Gutiérrez, L.; Morales, M. P.; Böhm, I. B.; Heverhagen, J. T.; Prospero, D.; Parak, W. J. *Chem. Soc. Rev.* **2012**, *41*, 4306–4334.
- (11) ISO. *ISO/TS 19807-1:2019 Nanotechnologies—Magnetic Nanomaterials—Part 1: Specification of Characteristics and Measurements for Magnetic Nanosuspensions*, 2019
- (12) Barrera, C.; Herrera, A. P.; Rinaldi, C. J. *Colloid Interface Sci.* **2009**, *329*, 107–113.
- (13) Saville, S. L.; Stone, R. C.; Qi, B.; Mefford, O. T. *J. Mater. Chem.* **2012**, *22*, 24909.
- (14) Krishnan, K. M.; Pakhomov, A. B.; Bao, Y.; Blomqvist, P.; Chun, Y.; Gonzales, M.; Griffin, K.; Ji, X.; Roberts, B. K. *J. Mater. Sci.* **2006**, *41*, 793–815.
- (15) Chantrell, R.; Popplewell, J.; Charles, S. *IEEE Trans. Magn.* **1978**, *14*, 975–977.
- (16) Kallumadil, M.; Tada, M.; Nakagawa, T.; Abe, M.; Southern, P.; Pankhurst, Q. A. *J. Magn. Magn. Mater.* **2009**, *321*, 1509–1513.
- (17) Maldonado-Camargo, L.; Unni, M.; Rinaldi, C. *Magnetic Characterization of Iron Oxide Nanoparticles for Biomedical Applications*. In *Biomedical Nanotechnology*; Springer, 2017; pp 47–71.
- (18) Goodhew, P. J.; Humphreys, J.; Beanland, R. *Electron Microscopy and Analysis*; Taylor & Francis, 2001.
- (19) Sridhara Rao, D. V.; Muralidharan, K.; Humphreys, C. J. TEM specimen preparation techniques. In *Microscopy: Science, Technology, Applications and Education*; Microscopy Series No. 4, Vol. 3, Formatex, 2010; pp 1232–1244.
- (20) *Image J*, <https://imagej.nih.gov/ij/>.
- (21) Kim, B. H.; Yang, J.; Lee, D.; Choi, B. K.; Hyeon, T.; Park, J. *Adv. Mater.* **2018**, *30*, 1703316.
- (22) Dai, L.; Schrand, A. M.; Hussain, S. M.; Schlager, J. J. *Nat. Protoc.* **2010**, *5*, 744–757.
- (23) Fabris, F.; Lima, E.; De Biasi, E.; Troiani, H. E.; Vázquez Mansilla, M.; Torres, T. E.; Fernández Pacheco, R.; Ibarra, M. R.; Goya, G. F.; Zysler, R. D.; Winkler, E. L. *Nanoscale* **2019**, *11*, 3164–3172.
- (24) Cali, E.; Qi, J.; Preedy, O.; Chen, S.; Boldrin, D.; Branford, W. R.; Vandeperre, L.; Ryan, M. P. *J. Mater. Chem. A* **2018**, *6*, 3063–3073.
- (25) Zheng, H.; Meng, Y. S.; Zhu, Y. *MRS Bull.* **2015**, *40*, 12–18.
- (26) Baumgartner, J.; Dey, A.; Bomans, P. H. H.; Le Coadou, C.; Fratzl, P.; Sommerdijk, N. A. J. M.; Faivre, D. *Nat. Mater.* **2013**, *12*, 310–314.
- (27) Bothun, G. D., PhD; Lelis, A., BS; Chen, Y., PhD; Scully, K., BS; Anderson, L. E., MS; Stoner, M. A., PhD *Nanomedicine* **2011**, *7*, 797–805.
- (28) Nwoko, K. C.; Raab, A.; Cheyne, L.; Dawson, D.; Krupp, E.; Feldmann, J. *J. Chromatogr. B: Anal. Technol. Biomed. Life Sci.* **2019**, *1124*, 356–365.
- (29) Hall, B. D.; Zanchet, D.; Ugarte, D. *J. Appl. Crystallogr.* **2000**, *33*, 1335–1341.
- (30) Tatarchuk, T.; Bououdina, M.; Macyk, W.; Shyichuk, O.; Paliychuk, N.; Yaremiy, I.; Al-Najar, B.; Pacia, M. *Nanoscale Res. Lett.* **2017**, *12*, 1–11.
- (31) Prabhu, Y. T.; Rao, K. V.; Kumar, V. S. S.; Kumari, B. S. *World J. Nano Sci. Eng.* **2014**, *04*, 21–28.
- (32) Rümenapp, C.; Wagner, F. E.; Gleich, B. J. *Magn. Magn. Mater.* **2015**, *380*, 241–245.
- (33) Hufschmid, R.; Arami, H.; Ferguson, R. M.; Gonzales, M.; Teeman, E.; Brush, L. N.; Browning, N. D.; Krishnan, K. M. *Nanoscale* **2015**, *7*, 11142–11154.
- (34) Pauw, B. R. *J. Phys.: Condens. Matter* **2014**, *26*, 239501.
- (35) Förster, S.; Apostol, L.; Bras, W. *J. Appl. Crystallogr.* **2010**, *43*, 639–646.
- (36) Borchert, H.; Shevchenko, E. V.; Robert, A.; Mekis, I.; Kornowski, A.; Grübel, G.; Weller, H. *Langmuir* **2005**, *21*, 1931–1936.
- (37) LaGrow, A. P.; Ingham, B.; Toney, M. F.; Tilley, R. D. *J. Phys. Chem. C* **2013**, *117*, 16709–16718.
- (38) Cannas, C.; Ardu, A.; Musinu, A.; Suber, L.; Ciasca, G.; Amenitsch, H.; Campi, G. *ACS Nano* **2015**, *9*, 7277–7286.
- (39) Fernández van Raap, M. B.; Mendoza Zélis, P.; Coral, D. F.; Torres, T. E.; Marquina, C.; Goya, G. F.; Sánchez, F. H. *J. Nanopart. Res.* **2012**, *14*, 1072.
- (40) Itri, R.; Depeyrot, J.; Tourinho, F. A.; Sousa, M. H. *Eur. Phys. J. E: Soft Matter Biol. Phys.* **2001**, *4*, 201–208.
- (41) Mühlbauer, S.; Honecker, D.; PéRigo, É A.; Bergner, F.; Disch, S.; Heinemann, A.; Erokhin, S.; Berkov, D.; Leighton, C.; Eskildsen, M. R.; Michels, A. *Rev. Mod. Phys.* **2019**, *91*, 015004.
- (42) Hore, M. J. A.; Ford, J.; Ohno, K.; Composto, R. J.; Hammouda, B. *Macromolecules* **2013**, *46*, 9341–9348.
- (43) Oberdick, S. D.; Abdelgawad, A.; Moya, C.; Mesbahi-Vasey, S.; Kepaptsoglou, D.; Lazarov, V. K.; Evans, R. F. L.; Meilak, D.; Skoropata, E.; van Lierop, J.; Hunt-Isaak, I.; Pan, H.; Ijiri, Y.; Krycka, K. L.; Borchers, J. A.; Majetich, S. A. *Sci. Rep.* **2018**, *8*, 3425.
- (44) Krycka, K. L.; Booth, R. A.; Hogg, C. R.; Ijiri, Y.; Borchers, J. A.; Chen, W. C.; Watson, S. M.; Laver, M.; Gentile, T. R.; Dedon, L. R.; Harris, S.; Rhyne, J. J.; Majetich, S. A. *Phys. Rev. Lett.* **2010**, *104*, 207203.

- (45) Narayanasamy, K. K.; Cruz-Acuña, M.; Rinaldi, C.; Everett, J.; Dobson, J.; Telling, N. D. *J. Colloid Interface Sci.* **2018**, *532*, 536–545.
- (46) Morgese, G.; Shirmardi Shaghasemi, B.; Causin, V.; Zenobi Wong, M.; Ramakrishna, S. N.; Reimhult, E.; Benetti, E. M. *Angew. Chem., Int. Ed.* **2017**, *56*, 4507–4511.
- (47) Provencher, S. W. *Comput. Phys. Commun.* **1982**, *27*, 229–242.
- (48) Provencher, S. W. *Comput. Phys. Commun.* **1982**, *27*, 213–227.
- (49) Koppel, D. E. *J. Chem. Phys.* **1972**, *57*, 4814–4820.
- (50) Lim, J.; Yeap, S. P.; Che, H. X.; Low, S. C. *Nanoscale Res. Lett.* **2013**, *8*, 381.
- (51) ISO. *Particle size analysis—Dynamic light scattering (DLS)*, ISO 22412:2017, 2017.
- (52) Di Silvio, D.; Rigby, N.; Bajka, B.; Mackie, A.; Baldelli Bombelli, F. *Int. J. Biochem. Cell Biol.* **2016**, *75*, 212–222.
- (53) Luo, P.; Roca, A.; Tiede, K.; Privett, K.; Jiang, J.; Pinkstone, J.; Ma, G.; Veinot, J.; Boxall, A. J. *Environ. Sci.* **2018**, *64*, 62–71.
- (54) *Guidelines for good practices in zeta-potential measurement*, PD ISO/TR 19997, 2018.
- (55) Andrew, J. S.; Rinaldi, C.; Mefford, O. T. *Synthesis and Surface Functionalization of Ferrite Nanoparticles*. In *Nanomagnetic Actuation in Biomedicine*; CRC Press, Vol. 1, pp 9–40.
- (56) ASTM International. *E394 Standard Test Method for Iron in Trace Quantities Using the 1,10-Phenanthroline Method*, 2015.
- (57) Olesik, J. W. *Anal. Chem.* **1991**, *63*, 12A–21A.
- (58) Zirbs, R.; Lassenberger, A.; Vonderhaid, I.; Kurzhals, S.; Reimhult, E. *Nanoscale* **2015**, *7*, 11216–11225.
- (59) Grunewald, T. A.; Lassenberger, A.; van Oostrum, P. D. J.; Rennhofer, H.; Zirbs, R.; Capone, B.; Vonderhaid, I.; Amenitsch, H.; Lichtenegger, H. C.; Reimhult, E. *Chem. Mater.* **2015**, *27*, 4763–4771.
- (60) Davis, K. M.; Qi, B.; Witmer, M.; Kitchens, C. L.; Powell, B. A.; Mefford, O. T. *Langmuir* **2014**, *30*, 10918–10925.
- (61) Davis, K.; Cole, B.; Ghelardini, M.; Powell, B. A.; Mefford, O. T. *Langmuir* **2016**, *32*, 13716–13727.
- (62) Yang, K.; Peng, H.; Wen, Y.; Li, N. *Appl. Surf. Sci.* **2010**, *256*, 3093–3097.
- (63) Oliveira, A.; Hnedá, M. L.; Fernandez-Outon, L. E.; de Sousa, E. M. B.; Ardisson, J. D. *Ceram. Int.* **2019**, *45*, 17920.
- (64) Žalneravičius, R.; Paškevičius, A.; Mažeika, K.; Jagminas, A. *Appl. Surf. Sci.* **2018**, *435*, 141–148.
- (65) Hwang, S. W.; Umar, A.; Dar, G. N.; Kim, S. H.; Badran, R. I. *Sens. Lett.* **2014**, *12*, 97–101.
- (66) Galinetto, P.; Albin, B.; Bini, M.; Mozzati, M. C. *Raman Spectroscopy* **2018**, No. InTech, 223.
- (67) Bergmann CP, P. P. *J. Mater. Sci. Eng.* **2015**, *5*, 217.
- (68) Shavel, A.; Rodríguez-González, B.; Spasova, M.; Farle, M.; Liz-Marzán, L. M. *Adv. Funct. Mater.* **2007**, *17*, 3870–3876.
- (69) Cullity, B. D.; Graham, C. D. *Introduction to Magnetic Materials*; Wiley-IEEE Press, 2008.
- (70) Foner, S. *Rev. Sci. Instrum.* **1959**, *30*, 548–557.
- (71) Clarke, J. SQUID (Superconducting Quantum Interference Device). In *AccessScience*; McGraw-Hill Education, 2014; DOI: 10.1036/1097-8542.649800.
- (72) Vallejo-Fernandez, G.; Whear, O.; Roca, A. G.; Hussain, S.; Timmis, J.; Patel, V.; O'Grady, K. *J. Phys. D: Appl. Phys.* **2013**, *46*, 312001.
- (73) Teja, A. S.; Koh, P. *Prog. Cryst. Growth Charact. Mater.* **2009**, *55*, 22–45.
- (74) Connord, V.; Mehdaoui, B.; Tan, R. P.; Carrey, J.; Respaud, M. *Rev. Sci. Instrum.* **2014**, *85*, 093904.
- (75) Mehdaoui, B.; Meffre, A.; Carrey, J.; Lachaize, S.; Lacroix, L.; Gougeon, M.; Chaudret, B.; Respaud, M. *Adv. Funct. Mater.* **2011**, *21*, 4573–4581.
- (76) Cabrera, D.; Lak, A.; Yoshida, T.; Materia, M. E.; Ortega, D.; Ludwig, F.; Guardia, P.; Sathya, A.; Pellegrino, T.; Teran, F. J. *Nanoscale* **2017**, *9*, 5094–5101.
- (77) Blanco-Andujar, C.; Teran, F. J.; Ortega, D. *Current Outlook and Perspectives on Nanoparticle-Mediated Magnetic Hyperthermia*. In *Iron Oxide Nanoparticles for Biomedical Applications*; Elsevier Ltd., 2018; Chapter 8, pp 197–245.
- (78) Livesey, K. L.; Ruta, S.; Anderson, N. R.; Baldomir, D.; Chantrell, R. W.; Serantes, D. *Sci. Rep.* **2018**, *8*, 11166.
- (79) Bruvera, I. J.; Mendoza Zelis, P.; Pilar Calatayud, M.; Goya, G. F.; Sanchez, F. H. *J. Appl. Phys.* **2015**, *118*, 184304.
- (80) Joy, P. A.; Kumar, P. A.; Date, S. K. *J. Phys.: Condens. Matter* **1998**, *10*, 11049.
- (81) del Castillo, E.; Santiago, E. *IEEE Trans. Magn.* **2010**, *43*, 54.
- (82) Connolly, J.; St Pierre, T. G. *J. Magn. Magn. Mater.* **2001**, *225*, 156–160.
- (83) Herrera, A. P.; Barrera, C.; Zayas, Y.; Rinaldi, C. *J. Colloid Interface Sci.* **2010**, *342*, 540–549.
- (84) Bohorquez, A. C.; Rinaldi, C. *Particle & Particle Systems Characterization* **2014**, *31*, 561–570.
- (85) Maldonado-Camargo, L.; Torres-Díaz, I.; Chiu-Lam, A.; Hernández, M.; Rinaldi, C. *J. Magn. Magn. Mater.* **2016**, *412*, 223–233.
- (86) Ludwig, F.; Balceris, C.; Jonasson, C.; Johansson, C. *IEEE Trans. Magn.* **2017**, *53*, 1–4.
- (87) Enpuku, K.; Tamai, Y.; Mitake, T.; Yoshida, T.; Matsuo, M. *J. Appl. Phys.* **2010**, *108*, 034701.
- (88) Fock, J.; Bogart, L. K.; González-Alonso, D.; Espeso, J. I.; Hansen, M. F.; Varón, M.; Frandsen, C.; Pankhurst, Q. A. *J. Phys. D: Appl. Phys.* **2017**, *50*, 265005.
- (89) Estelrich, J.; Sánchez-Martín, M. J.; Busquets, M. A. *Int. J. Nanomed.* **2015**, *10*, 1727–1741.
- (90) Henoumont, C.; Laurent, S.; Vander Elst, L. *Contrast Media Mol. Imaging* **2009**, *4*, 312–321.
- (91) Chavhan, G. B.; Babyn, P. S.; Thomas, B.; Shroff, M. M.; Haacke, E. M. *RadioGraphics* **2009**, *29*, 1433–1449.
- (92) Henoumont, C.; Laurent, S.; Vander Elst, L. *Contrast Media Mol. Imaging* **2009**, *4*, 312–321.
- (93) Thorek, D.; Chen, A.; Czupryna, J.; Tsourkas, A. *Ann. Biomed. Eng.* **2006**, *34*, 23–38.
- (94) Gordon, R. T.; Hines, J. R.; Gordon, D. *Med. Hypotheses* **1979**, *5*, 83–102.
- (95) Matsuoka, F.; Shinkai, M.; Honda, H.; Kubo, T.; Sugita, T.; Kobayashi, T. *BioMag. Res. Technol.* **2004**, *2*, 3.
- (96) Yanase, M.; Shinkai, M.; Honda, H.; Wakabayashi, T.; Yoshida, J.; Kobayashi, T. *Jpn. J. Cancer Res.* **1998**, *89*, 775–782.
- (97) Ito, A.; Shinkai, M.; Honda, H.; Yoshikawa, K.; Saga, S.; Wakabayashi, T.; Yoshida, J.; Kobayashi, T. *Cancer Immunol. Immunother.* **2003**, *52*, 80–88.
- (98) Maier-Hauff, K.; Ulrich, F.; Nestler, D.; Niehoff, H.; Wust, P.; Thiesen, B.; Orawa, H.; Budach, V.; Jordan, A. *J. Neuro-Oncol.* **2011**, *103*, 317–324.
- (99) Johannsen, M.; Gneveckow, U.; Eckelt, L.; Feussner, A.; Wald ofner, N.; Scholz, R.; Deger, S.; Wust, P.; Loening, S. A.; Jordan, A. *Int. J. Hyperthermia* **2005**, *21*, 637–647.
- (100) Gneveckow, U.; Jordan, A.; Scholz, R.; Bruß, V.; Waldofner, N.; Ricke, J.; Feussner, A.; Hildebrandt, B.; Rau, B.; Wust, P. *Med. Phys.* **2004**, *31*, 1444.
- (101) Thiesen, B.; Jordan, A. *Int. J. Hyperthermia* **2008**, *24*, 467–474.
- (102) Grazil, V.; Silber, A. M.; Moros, M.; Asin, L. *Int. J. Nanomed.* **2012**, *7*, 5351–5360.
- (103) Raval, Y. S.; Fellows, B. D.; Murbach, J.; Cordeau, Y.; Mefford, O. T.; Tzeng, T. J. *Adv. Funct. Mater.* **2017**, *27*, 1701473.
- (104) Goya, G. F.; Asin, L.; Ibarra, M. R. *Int. J. Hyperthermia* **2013**, *29*, 810–818.
- (105) Villanueva, A.; de la Presa, P.; Alonso, J. M.; Rueda, T.; Martínez, A.; Crespo, P.; Morales, M. P.; Gonzalez-Fernandez, M. A.; Valdes, J.; Rivero, G. *J. Phys. Chem. C* **2010**, *114*, 1976–1981.
- (106) Sanchez, C.; El Hajj Diab, D.; Connord, V.; Clerc, P.; Meunier, E.; Pipy, B.; Payre, B.; Tan, R. P.; Gougeon, M.; Carrey, J.; Gigoux, V.; Fourmy, D. *ACS Nano* **2014**, *8*, 1350–1363.
- (107) Domenech, M.; Marrero-Berrios, I.; Torres-Lugo, M.; Rinaldi, C. *ACS Nano* **2013**, *7*, 5091–5101.
- (108) Creixell, M.; Bohorquez, A. C.; Torres-Lugo, M.; Rinaldi, C. *ACS Nano* **2011**, *5*, 7124–7129.

- (109) Kozissnik, B.; Bohorquez, A. C.; Dobson, J.; Rinaldi, C. *Int. J. Hyperthermia* **2013**, *29*, 706–714.
- (110) Carrey, J.; Mehdaoui, B.; Respaud, M. *J. Appl. Phys.* **2011**, *109*, 083921.
- (111) Serantes, D.; Simeonidis, K.; Angelakeris, M.; Chubykalo-Fesenko, O.; Marciello, M.; Morales, M. d. P.; Baldomir, D.; Martinez-Boubeta, C. *J. Phys. Chem. C* **2014**, *118*, 5927–5934.
- (112) Eggeman, A. S.; Majetich, S. A.; Farrell, D.; Pankhurst, Q. A. *IEEE Trans. Magn.* **2007**, *43*, 2451–2453.
- (113) Dutz, S.; Hergt, R. *Nanotechnology* **2014**, *25*, 452001.
- (114) Dennis, C. L.; Ivkov, R. *Int. J. Hyperthermia* **2013**, *29*, 715–729.
- (115) Dennis, C. L.; Krycka, K. L.; Borchers, J. A.; Desautels, R. D.; van Lierop, J.; Huls, N. F.; Jackson, A. J.; Gruettner, C.; Ivkov, R. *Adv. Funct. Mater.* **2015**, *25*, 4300–4311.
- (116) Atkinson, W. J.; Brezovich, I. A.; Chakraborty, D. P. *IEEE Trans. Biomed. Eng.* **1984**, *BME-31*, 70–75.
- (117) Merida, F.; Chiu-Lam, A.; Bohorquez, A. C.; Maldonado-Camargo, L.; Perez, M.-E.; Pericchi, L.; Torres-Lugo, M.; Rinaldi, C. *J. Magn. Mater.* **2015**, *394*, 361–371.
- (118) Andreu, I.; Natividad, E. *Int. J. Hyperthermia* **2013**, *29*, 739–751.
- (119) Dutz, S.; Hergt, R. *Int. J. Hyperthermia* **2013**, *29*, 790–800.
- (120) Fadeel, B.; Farcas, L.; Hardy, B.; Vázquez-Campos, S.; Hristozov, D.; Marcomini, A.; Lynch, I.; Valsami-Jones, E.; Alenius, H.; Savolainen, K. *Nat. Nanotechnol.* **2018**, *13*, 537–543.
- (121) Sukhanova, A.; Bozrova, S.; Sokolov, P.; Berestovoy, M.; Karaulov, A.; Nabiev, I. *Nanoscale Res. Lett.* **2018**, *13*, 44.